Effective permittivity and third-order nonlinear susceptibility for a dilute composite consisting of partially aligned nanorods

Yedidya Lior* and Dan M. Marom

Applied Physics Department, Hebrew University, Jerusalem 91904, Israel
**Corresponding author: yedidya.lior@mail.huji.ac.il*

Received February 20, 2013; revised May 15, 2013; accepted May 15, 2013;
posted May 20, 2013 (Doc. ID 185561); published June 13, 2013

The expected permittivity and third-order nonlinear susceptibility of a composite consisting of semiconductor nanorods (NRs) dispersed in a polymer host are derived using a generalized Maxwell Garnett model under various NR axis orientation statistics, achieved by an aligning electric field. The semiconductor NRs are analyzed as prolate spheroids and modeled as more realistic capsule shapes. From the angular distribution function of the NRs, the composite macroscopic characteristics are found for low filling fractions. As the alignment field strength increases, the composite optical properties asymptotically converge toward the nematic case. Aligning fields of order 10^7 V/m are required for the optical properties to increase to half the value between random orientation and nematic array composites. © 2013 Optical Society of America

OCIS codes: (160.4236) Nanomaterials; (160.4330) Nonlinear optical materials.
http://dx.doi.org/10.1364/JOSAB.30.001864

1. INTRODUCTION

The physical properties of nanoparticles can be significantly manipulated by controlling their shape to match specific needs. Rod-shaped nanocrystals exhibit an enhanced optical response along their long axis (LA) due to surface polarization [1,2]. Composites consisting of such nanorods (NRs) embedded in a dielectric host can serve as building blocks for various optical applications. For example, composites from spherical nanoparticles embedded in perfluorocyclobutane (PFCB) polymer were proven to be suitable for optical waveguides [3,4]. In addition, TiO_2 NRs inside poly (methyl methacrylate) were shown to be good candidates for nonlinear (NL) optical composite media [5].Choosing the right host material can provide a composite with optical characteristics fit for optical applications, such as optical waveguides. Dispersing NRs with specific characteristics, such as strong nonlinearity and a suitable bandgap inside the host can provide tunable composite properties that depend on the material choice and dimensions of the NRs on the one hand and on the statistical directionality of the NRs in the composite on the other hand.

Quantitative models that analyze composites with embedded NRs are mostly based on describing NRs as prolate spheroids in a perfect nematic array [Fig. 1(a)], where no statistical measure of the NR alignment spread in the composite is discussed [6–9]. A nematic configuration can be fabricated in planar (2D) arrays by various techniques, such as electron-beam lithography [10], nanosphere lithography [11], and colloidal self-assembly for both vertically [12] and horizontally [13] positioned NRs. In a volumetric (3D) array, achieving control over the directionality is problematic, and thus it is much harder to fabricate a perfect nematic array. The case of random orientation [Fig. 1(b)] was also addressed and compared to the nematic case for linear material properties [7–9]. The case of statistical orientation [Fig. 1(c)] was addressed theoretically for the linear regime with an arbitrary distribution function, without analysis or calculations related to the origin of the alignment or the statistical alignment spread's influence on the resulting macroscopic characteristics [7,9]. For the statistical case, a qualitative description of composites' macroscopic characteristics was given in terms of the volume the NRs occupy in the composite, rather than the whole composite characteristics [14].

We present a comprehensive quantitative statistical model for calculating the macroscopic characteristics of such composites and finding their permittivity and third-order NL susceptibility. The model takes into account several factors that were previously ignored: the geometry of a single NR is described as a capsule, which better matches most NRs transmission electron microscopy images and the statistical behavior of the NR alignment in the composite under an applied electric field for cases with and without a permanent electrical dipole moment in the NRs. We consider nonresonant optical excitation of the NRs, hence making the inclusion material properties of permittivity and NL susceptibility real (negligible single- and multiple-photon absorption) and wavelength independent. This can be realized by choosing an inclusion material and size with a sufficiently high bandgap energy relative to the photoexcitation energy. In addition, we ignore any quantum confinement effects for simplicity, although they can be taken into account by using a size-dependent permittivity [15,16].

2. PERMITTIVITY AND NONLINEAR SUSCEPTIBILITY OF A COMPOSITE WITH NANORODS

The macroscopic properties of dilute composites are classically described by the Maxwell Garnett (MG) model, which

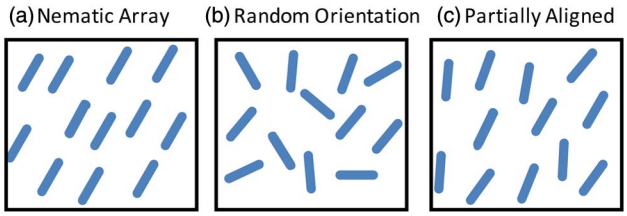

Fig. 1. Illustrations describing different NRs alignment degrees: (a) perfect nematic array of NRs, (b) randomly distributed NRs, and (c) partially aligned NRs.

deals with a dilute composite of linear spherical inclusions embedded in a linear dielectric medium [17]. The limit for the dilute mixture is usually set as 20% volume fraction [6]. The dilute limit ensures that there is no interaction between the NRs and that the composite can be treated as a continuum, provided the optical wavelength of the electric field is sufficiently large [7,18]. For the linear regime, we use a generalization of the MG model, which deals with ellipsoidal inclusions [6–8]. The ellipsoidal inclusions are all parallel (nematic array), and the model describes the macroscopic characteristics when the composite is examined in a direction parallel to any major axis of the array of ellipsoids. We use the presentation of the effective permittivity, ε_{eff}, of such a composite that is given by Sihvola [7]:

$$\varepsilon_{\text{eff}}^{j} = \varepsilon_h + p\varepsilon_h \frac{\varepsilon_i - \varepsilon_h}{\varepsilon_h + L^j(1-p)(\varepsilon_i - \varepsilon_h)}, \tag{1}$$

where ε_h, ε_i are the host and inclusions permittivity, respectively, L^j is the depolarization factor of the ellipsoid in the $j = x, y, z$ direction, which is a geometrical factor that express the different electrostatic response of the ellipsoid under an electric field along the ellipsoid axes, and p is the volume fraction of the inclusions in the composite. For a general ellipsoid (three different semi-axes), the expression for L^j has an integral form without a closed form solution [7,19].

In the case of prolate spheroids [an ellipsoid with one LA and two equal short axes (SAs), see Fig. 2(a)], there is a closed form for the depolarization factor. Assuming that the three semi-axes of the prolate spheroid are $a_x = a_y < a_z$ ($\hat{\mathbf{z}}$ is the LA of the prolate spheroid), the depolarization factors are [7]

$$L^z = \frac{1-e^2}{e^2}\left[\frac{1}{2e}\ln\left(\frac{1+e}{1-e}\right) - 1\right], \qquad L^x = L^y = \frac{1-L^z}{2}, \tag{2}$$

where $e = \sqrt{1 - a_x^2/a_z^2}$ is the eccentricity of the prolate spheroid. Due to the existence of an analytic solution and the approximate similarity to the shape of NRs, prolate spheroid shapes have been used previously to model the properties of composites with NR inclusions.

It will be instructive to further describe the characteristic of a single NR, i.e., the polarizability α, which is a measurement of the internal induced dipole moment. The polarizability is defined by $\boldsymbol{\mu} = \bar{\bar{\boldsymbol{\alpha}}} \cdot \mathbf{E}_{\text{ext}}$, where $\mathbf{E}_{\text{ext}}$ is an externally applied electric field and $\boldsymbol{\mu}$ is the induced dipole moment within the inclusion. In the general case for an ellipsoid, $\bar{\bar{\boldsymbol{\alpha}}}$ is a second-rank tensor, and when treating the NRs' constituent material as isotropic, $\bar{\bar{\boldsymbol{\alpha}}}$ reduces to a diagonal $[3 \times 3]$ matrix. The diagonal elements differ from one another due to the geometry of the inclusion. We follow again the derivation of Sihvola [7], and these three diagonal elements are

$$\alpha^j = \frac{V(\varepsilon_i - \varepsilon_h)}{\varepsilon_h + L^j(\varepsilon_i - \varepsilon_h)}\varepsilon_h, \tag{3}$$

where V is the volume of the ellipsoid and again $j = x, y, z$. For a prolate spheroid, the elements in the two SA directions ($\hat{\mathbf{x}}$ and $\hat{\mathbf{y}}$) are equal. It is worth noting that an alternate form for Eq. (3), presented by Landau and Lifshitz, does not have the last multiplication by ε_h [19]. We follow Sihvola's notation, which perfectly matches our simulation results, presented in Section 3.

For the NL regime, there are several different derivations for the third-order NL susceptibility of the composite [6,7,18]. We follow again the derivation of Sihvola [7], starting from describing the single NR contribution. The NL characteristics of the NR can be found by a perturbative approach that uses the hyperpolarizability of the ellipsoid, which describes the NL response of the dipole moment in the ellipsoid caused by an electric field. Sihvola presents the results for the first- and second-order hyperpolarizability, $\bar{\bar{\boldsymbol{\beta}}}$ and $\bar{\bar{\boldsymbol{\gamma}}}$, respectively. We shall ignore the first-order hyperpolarizability, which occurs in noncentrosymmetric crystals with second-order response ($\chi^{(2)}$). Sihvola explicitly presents the hyperpolarizability for a sphere inclusion by expanding the internal field inside the sphere in a power series. Following the same derivation technique, with the internal field for an ellipsoid, we calculate the third-order hyperpolarizability for ellipsoid inclusions as

$$\gamma^j = \left[\frac{\varepsilon_h}{\varepsilon_h + L^j(\varepsilon_i - \varepsilon_h)}\right]^4 \varepsilon_0 V \chi_i^{(3)}, \tag{4}$$

where $\chi_i^{(3)}$ is the third-order NL susceptibility of the inclusion material. Its tensorial characteristics will be addressed below, and we assume linear behavior of the host material. For the whole composite with small volume fraction (typically $p \ll 1$), the effective third-order NL susceptibility is

$$\chi_{\text{eff}}^{(3),j} = \frac{n\gamma^j}{\varepsilon_0} = p\left[\frac{\varepsilon_h}{\varepsilon_h + L^j(\varepsilon_i - \varepsilon_h)}\right]^4 \chi_i^{(3)}, \tag{5}$$

where n is the number density of inclusions, i.e., $p = nV$. It is important to note that since we assumed nonresonant excitation, hence ignoring single- or multiple-photon absorption, we consider only real values for the host and inclusion permittivities and NL susceptibilities. The derivations for a material with complex properties can be evaluated by slightly modifying Eq. (5) following Ref. [6]. By doing so, the imaginary parts of the NL susceptibilities can also be found; hence NL absorption can be addressed, but this is beyond the scope of this study. Lamarre *et al.* derived, in addition to Eq. (5), an equation for larger volume fraction p (up to the MG model limit), which includes an additional expression $pL^j(\varepsilon_i - \varepsilon_h)$ in the denominator [6], but we will restrict ourselves to small volume fraction only. It is important to note that the depolarization factor decreases when the axes aspect ratio (AR) of the spheroid increases, indicating a stronger polarization inside the inclusion. Hence, the effective permittivity [Eq. (1)], the polarizability [Eq. (3)] and the effective third-order NL

susceptibility [Eq. (5)] increase along the LA direction when the AR increases.

There are two assumptions made in Eqs. (1) and (5) that we wish to address:

(1) Most transmission electron microscopy images reveal that a prolate spheroid shape [Fig. 2(a)] is not an accurate descriptor for colloidal NR (e.g., see images in [20,21]). Their shape is better described by a capsule shape, a cylinder with hemisphere capping [Fig. 2(b)]. Pecharromán *et al.* analyzed the geometry of NRs meticulously and noted that the structure is even more complicated [20]; they showed that the capping is not exactly a hemisphere and also referred to the roughness of the surface. We shall ignore such factors for simplicity.

(2) These formulas were derived for a perfect nematic array of NRs with an electric field parallel to a major axis of the spheroids and ignore any statistical alignment distribution.

3. PROLATE SPHEROID VERSUS CAPSULE SHAPE

To better understand the different electrostatic characteristics of the two shapes, we compared the polarizability of the capsule shape to that of the prolate spheroid. The induced dipole moment is found by simulating a nanoinclusion inside a uniform external field $\mathbf{E}_{\text{ext}}$, using electrostatic finite element analysis with Comsol Multiphysics simulation software, and by calculating the induced dipole moment as [7]

$$\boldsymbol{\mu} = (\varepsilon_i - \varepsilon_h) \int \mathbf{E}_{\text{in}} \cdot \mathrm{d}V, \tag{6}$$

where $\mathbf{E}_{\text{in}}$ is the electric field inside the inclusion, which is provided by the finite element analysis simulation. The polarizability $\bar{\bar{\boldsymbol{\alpha}}}$ can now be extracted, since we have the relationship between the external field and the induced dipole moment. It is worth mentioning that finite element simulations result in minute induced dipole moment components in the directions perpendicular to the external field (6 orders of magnitude smaller). These are considered a numeric artifact (as symmetric shapes in uniform field parallel to a major axis cannot have polarizability components in orthogonal directions), and we neglected them. We compared the simulation results of the capsule shape to prolate spheroids, with the same length and width, as shown in Fig. 2. The finite element analysis simulation results are presented in Table 1. We also present in Table 1 the value of the polarizability normalized by the volume to estimate the average polarization density inside the inclusions, which will be important for estimating the depolarization factor. The

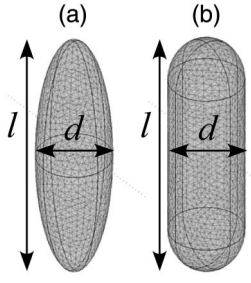

Fig. 2. Illustration depicting (a) the prolate spheroid shape and (b) the capsule shape proposed to describe the geometry of NRs. Both shapes have the same length ($l = 2 \cdot a_z$) and diameter ($d = 2 \cdot a_x$).

Table 1. Polarizability of Prolate Spheroids and Capsule Shape for Different Dimensions, Axes Aspect Ratio, and Average Polarization Density

			$\alpha/(4\pi\varepsilon_0)$ [nm^3]		$[\alpha/(4\pi\varepsilon_0)]/V$	
l [nm]	d [nm]	Aspect Ratio	Prolate Spheroid	Capsule	Prolate Spheroid	Capsule
8	2	4	8.35	11.21	0.499	0.487
40	10		1044	1402		
40	8	5	704	958	0.525	0.511
60	12		2377	3234		
40	4	10	195	274	0.582	0.564
60	6		659	924		
140	14		8367	11,742		

simulations and calculations were performed for CdSe NRs inside PFCB polymer host and use the material properties at optical frequencies ($\varepsilon_i = 6.2, \varepsilon_h = 2.19$).

The simulation results for the prolate spheroid match the analytical results of Eq. (3) (0.03% error). The polarizability of identical axis dimensions of capsule shapes is larger by 35%–45% compared to the prolate spheroids, indicating that the dipole moment created in the nanocrystal will be larger as well. On the other hand, the normalized polarizability of the capsule shape is 1.5%–2.5% smaller than that of the prolate spheroid, leading to a lower average polarization density. The larger capsule polarizability is attributed to its larger volume compared to that of the spheroid, with the same length and width. In addition, we see the normalized polarizability grows with the AR.

In order to use Eqs. (1) and (3)–(5) with capsule-shaped inclusions, their depolarization factor must be found. This is done by finding an equivalent prolate spheroid based on the polarization density for each capsule shape. Using the results for the normalized polarizability of the capsule shapes inside Eq. (3) (which was developed for prolate spheroids), we extract the depolarization factor. By doing so, we treat the capsule shape as a prolate spheroid for the purpose of finding an effective depolarization factor. It is important to note that the single shape volume is not relevant for the calculation of the effective permittivity [Eqs. (1)] and effective susceptibility [Eq. (5)] rather the volume fraction. This means that for a given volume fraction the important value is the polarization density or the normalized polarizability of the single inclusion.

4. ALIGNMENT MECHANISM AND STATISTICAL BEHAVIOR

We next address the alignment mechanism and the statistical behavior of the NR angular orientation. The common alignment mechanism for suspended NRs in a fluid mixture is a strong external electric field $\mathbf{E}_{\text{align}}$. We examine a NR tilted at an angle θ to an external field [Fig. 3(a)]. The aligning field induces a dipole moment $\boldsymbol{\mu}$ in the NR. The interaction between the induced dipole moment and the original external field will cause a rotating moment $\mathbf{M} = \boldsymbol{\mu} \times \mathbf{E}_{\text{align}}$ acting on the NR [Fig. 3(b)], which is angle θ dependent. In a rotationally symmetric shape (e.g., spheroids and capsule shapes), the interaction is defined in a plane containing the vectors of the aligning field and the axis of symmetry of the shape (the LA in our case) [19]. Without loss of generality, we define the $\hat{\mathbf{z}}$ axis in the direction of the aligning field. The azimuthal angle

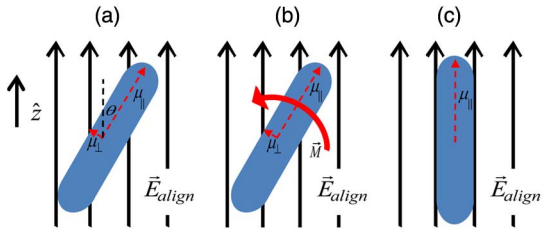

Fig. 3. Illustration depicting the alignment mechanism of the NRs by a DC electric field. (a) The aligning field causes induced dipole moments $\mu_{||}$, $\mu_{\perp}$ along NR major axes, parallel and normal to the NR LA, respectively. (b) The induced dipole moments cause a rotating moment **M** that acts on the NR. (c) The rotating moment tends to align the NR parallel to the aligning field.

(rotation about the $\hat{\mathbf{z}}$ axis) is irrelevant for the orientation analysis. The induced dipole moment in the NR has parallel and transverse components, $\mu_{||}$ and $\mu_{\perp}$, respectively:

$$\mu_{\parallel} = \alpha_{\parallel} E_{\text{align}} \cos\theta, \qquad \mu_{\perp} = \alpha_{\perp} E_{\text{align}} \sin\theta, \tag{7}$$

where $\alpha_{\parallel}$, $\alpha_{\perp}$ are the NR polarizabilities in the parallel and perpendicular directions, respectively. In dielectric and semiconductor NRs, for an elongated objects, such as prolate spheroids and capsules, $\mu_{||} > \mu_{\perp}$; hence the rotating moment will tend to align the NR parallel to the electric field [Fig. 3(c)], which is a stable point [14,19]. Note that we use a DC electric field for the alignment mechanism and focus on the steady-state solution; hence the effect of host viscosity is disregarded [14].

Another mechanism that can enhance the NRs' alignment is the presence of a permanent dipole moment (PDM), which occurs, for example, in wurtzite lattice structure NRs [22,23]. The PDM assists the alignment by enhancing the rotating moment acting on the single NR. This is especially important for aligning during the thermal polymerization of polymers taking place at elevated temperature (PFCB thermally polymerizes at 150°C–180°C). Li and Alivisatos estimated the PDM in wurtzite lattice CdSe NRs to be 100–200 Debye [22]. They showed that the magnitude of the PDM also grows linearly with the volume of the NR. For the same NR dimensions with a field of 5×10^6 V/m, the PDM is 3–6 times larger than the induced dipole moment. Their calculations are based on transient electric birefringence curves, where the ratio of PDM to the polarizability anisotropy (denoted γ in their work) is found from the curves. They also treated the NRs as prolate spheroids, for both volume and polarizability calculations with the Landau and Lifshitz formula. We applied our results for the capsule shape polarizability to their data, instead of those of the prolate spheroid. We estimate the PDM to be around 1.6 times larger than their estimations (up to 330 Debye) owing to the larger polarizability of the capsule shape over the prolate spheroid shape, due to the larger volume. Results for the PDM are presented in Table 2.

Combining the induced dipole moments and PDMs, the rotating moment that acts on the NRs will be

$$M = |\boldsymbol{\mu} \times \mathbf{E}_{\text{align}}| = \frac{1}{2}(\alpha_{\parallel} - \alpha_{\perp}) E_{\text{align}}^2 \sin 2\theta + \mu_p E_{\text{align}} \sin\theta. \tag{8}$$

We ignore the influence of the hyperpolarizability on the induced dipole moment and hence on the rotation moment for simplicity. Based on the rotating moment, we can calculate

Table 2. Comparison of Results of the PDM of the NRs Calculated by Li and Alivisatos[a] to Those in Our Analysis

l(nm)	d(nm)	μ, Prolate Spheroid[a] [Debye]	μ, Capsule [Debye]
30	4.8	209.9	329.8
60	3.1	153.4	249.9
54	3	126.3	205.4
23	3.8	126.4	198.3
35	3	95.7	153.7

[a]See [22]; we used the same parameters as presented in [22]: permittivity for the NRs' LAs and SAs $\varepsilon_{||} = 10.2$, $\varepsilon_{\perp} = 9.33$, and permittivity of the environment $\varepsilon_h = 2.02$.

the angular distribution function (ADF) of the NRs under such a field, following the method presented by Ruda and Shik [14]:

$$\text{ADF}(\theta) = \frac{\exp\left[-\frac{U_{\text{NR}}(\theta)}{K_B T}\right]}{\int_0^{\pi} \exp\left[-\frac{U_{\text{NR}}(\hat{\theta})}{K_B T}\right] \sin\hat{\theta} \mathrm{d}\hat{\theta}}, \tag{9}$$

where $U_{\text{NR}}(\theta) = \int_0^{\theta} M(\tilde{\theta}) \mathrm{d}\tilde{\theta}$ is the potential energy of a single NR under an electric field $\mathbf{E}_{\text{align}}$ at an angle θ to the LA of the NR [24]. The potential energy is at minimum when the NR is parallel to the external electric field, i.e., $\theta = 0$, and hence would tend to settle there, yet is perturbed by thermal fluctuations. Ruda and Shik's findings are also based on describing NRs as prolate spheroids, and they used the polarizability formula given by Landau and Lifshitz as previously discussed. It is important to note that the induced dipose moments and PDMs grow linearly with the NR volume, which causes the rotation moment to increase as well. Hence, the volume of a single NR is significant to the alignment mechanism, and larger NRs will have a greater rotation moment due to their larger volume.

In Fig. 4 we present the ADFs for a 30×4.8 nm NR, which has the largest PDM value of those presented in Table 2. The alignment process is by a DC electric field; hence the permittivities for the CdSe NRs and for the host PFCB were taken as $\varepsilon_{\text{CdSe},||} = 10.2$ $\varepsilon_{\text{CdSe},\perp} = 9.33$ (data taken from [22]) and $\varepsilon_{\text{PFCB}} = 2.4$. We can see the more significant alignment of the capsule shape (solid curves) compared to the prolate spheroid shape (discrete markers) for strong aligning fields, for NRs with and without PDM [Figs. 4(b) and 4(a), respectively], resulting from their larger polarizability (which evolves from their large volume) and hence larger dipole moment. We also see the ADF symmetry about $\theta = \pi/2$ in the case of NRs without PDM [Fig. (a)], in contrast to NRs with PDM [Figs. 4(b)–4(d)]. For an induced dipole moment, the two LA ends of the NR are indistinguishable because of the symmetry of the geometry; hence there is a symmetry for a rotation in $\theta = \pi$. With the PDM, there is only one alignment allowed to the external electrical field; hence the symmetry is broken.

Note the scale range for the NRs with PDM [Fig. 4(b)] is much larger compared to NRs without it [Fig. 4(a)], due to the stronger rotating moment and hence alignment, in the presence of PDM. We can further see that alignment at lower temperature is stronger [Fig. 4(c)] because of the suppressed thermal motion and for NRs with larger volume [Fig. 4(d)]

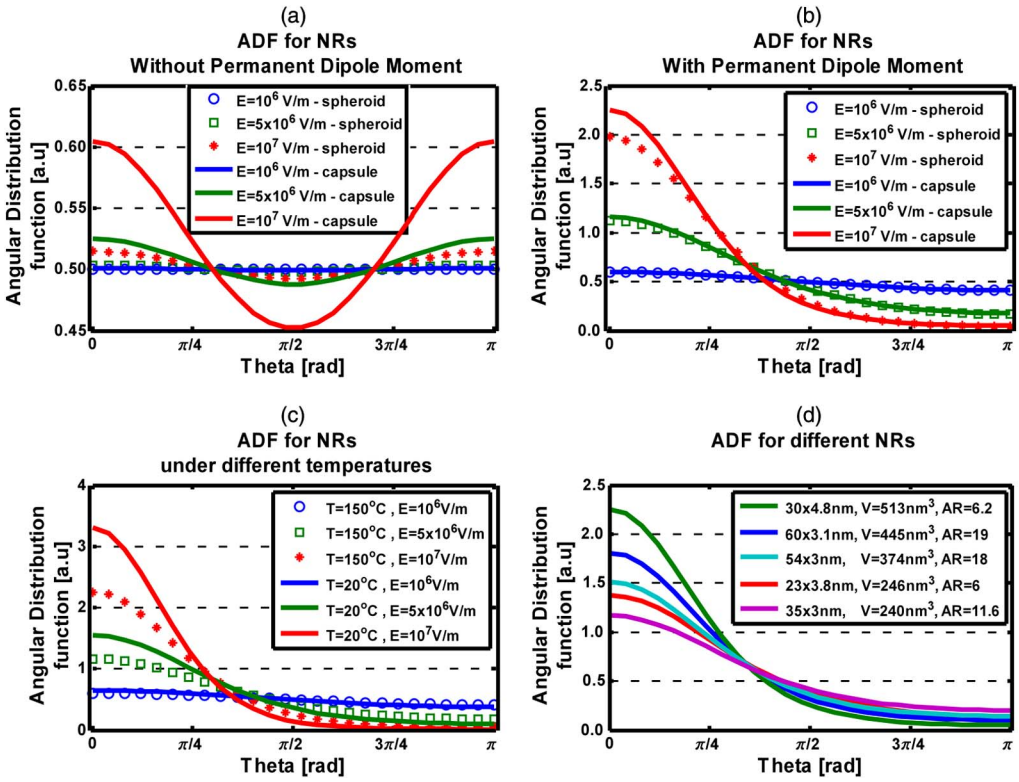

Fig. 4. (a) ADF of CdSe NRs without PDM inside PFCB: capsule shape versus prolate spheroid for different aligning electric field strengths under a temperature of 150°C, l = 30 nm, d = 4.8 nm. (b) The same for NRs with PDM. (c) Temperature dependency for different aligning fields (with PDM). (d) Different NRs with different volumes (for the NRs presented in Table 2, with PDM).

because of the larger induced dipole moments and PDMs, which enhance the rotating moment.

5. PERMITTIVITY AND NONLINEAR SUSCEPTIBILITY OF A COMPOSITE WITH STATISTICAL ALIGNMENT

With the NRs' ADF, we can now calculate the permittivity and third-order NL susceptibility of the mixture. For the permittivity of a nematic NR array, it is useful to notice that the effective permittivity [Eq. (1)] can be presented as a function of the normalized polarizability [7]:

$$\varepsilon_{\text{eff}}^{j} = \varepsilon_h + \varepsilon_h \frac{p(\alpha^j/V)}{\varepsilon_h - p(L^j\alpha^j/V)}, \tag{10}$$

where again p is the volume fraction and the depolarization factor, L^j, determines the composite anisotropy. The inclusion permittivity is expressed through the polarizability components α^j. Sihvola and Kong presented the permittivity in the case of a general angular distribution and used dyadic notation [9]. Using the notation of a second-rank tensor, the permittivity is a $[3\times 3]$ matrix. Addressing the whole partially aligned array, a single NR in the array will have an arbitrary orientation with angle θ about the $\hat{\mathbf{z}}$ axis and azimuthal angle φ about the $\hat{\mathbf{x}}$ axis, as illustrated in Fig. 5. The aligning field is set along the $\hat{\mathbf{z}}$ axis, as before.

To find the contribution of a single NR to the global composite response, we rotate our coordinate system to the local coordinate system of the NR, apply the polarizability tensor, and rotate the result back to the global coordinate system. In the local NR coordinate system, the polarizability tensor is

$$\bar{\bar{\boldsymbol{\alpha}}}_{\text{NR}} = \begin{pmatrix} \alpha_\perp & 0 & 0 \\ 0 & \alpha_\perp & 0 \\ 0 & 0 & \alpha_\parallel \end{pmatrix}, \tag{11}$$

and the depolarization factor in a tensorial presentation is

$$\bar{\bar{\mathbf{L}}}_{\text{NR}} = \begin{pmatrix} L_\perp & 0 & 0 \\ 0 & L_\perp & 0 \\ 0 & 0 & L_\parallel \end{pmatrix}, \tag{12}$$

where the subscript NR indicates the local coordinate system of the NR. We can treat $\bar{\bar{\boldsymbol{\alpha}}}_{\text{NR}}$ and $\bar{\bar{\mathbf{L}}}_{\text{NR}}$ as operators and denote

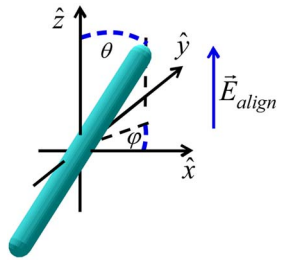

Fig. 5. Illustration for the coordinate system and the definition of the angles φ and θ describing the NR orientation. The aligning field is also presented.

rotation operators around the $\hat{\mathbf{z}}$ and $\hat{\mathbf{y}}$ axes as $\hat{\mathbf{R}}_z(\varphi)$ and $\hat{\mathbf{R}}_y(\theta)$, respectively, to set the azimuthal angle and NR tilt. A general operator $\mathbf{A}$, in the global coordinate system, will therefore be

$$\mathbf{A}_{xyz}(\varphi,\theta) = \hat{\mathbf{R}}_z(-\varphi)\hat{\mathbf{R}}_y(-\theta)\mathbf{A}_{\mathrm{NR}}\hat{\mathbf{R}}_y(\theta)\hat{\mathbf{R}}_z(\varphi), \tag{13}$$

where the subscript xyz indicates the global coordinate system. We then perform a weighted average using the ADF over the solid angle, spanning all possible angular orientations. The averaging is performed by integration over the azimuthal angle φ on the interval $[0, 2\pi]$ with a normalization of $1/2\pi$ (uniform distribution) and over the tilt angle θ on the interval $[0, \pi]$ with the distribution function—ADF(θ) [25]. The statistically weighted result is denoted $\langle \mathbf{A}_{xyz}\rangle_{\theta,\varphi}$ in the global coordinate system, and the result for the average permittivity is

$$\bar{\bar{\varepsilon}}_{\mathrm{eff}} = \varepsilon_h\bar{\bar{\mathbf{I}}} + \varepsilon_h\frac{p\langle\bar{\bar{\boldsymbol{\alpha}}}_{xyz}/V\rangle_{\theta,\varphi}}{\varepsilon_h\bar{\bar{\mathbf{I}}} - p\langle(\bar{\bar{\mathbf{L}}}\cdot\bar{\bar{\boldsymbol{\alpha}}})_{xyz}/V\rangle_{\theta,\varphi}}, \tag{14}$$

where $\bar{\bar{\mathbf{I}}}$ is the unit matrix, and the result is again a second-rank tensor. Performing the integration over φ eliminates all off-diagonal terms as a result of the uniform distribution, and we are left with a diagonal matrix, where the values in the x and y directions are equal. This enables us to present the results of the two independent elements in the different directions separately. The results after integration over φ and prior to integration over θ are

$$\begin{aligned}\varepsilon_{\mathrm{eff}}^{z} &= \varepsilon_h + \varepsilon_h\frac{p\langle\alpha_{\parallel}\cos^2\theta + \alpha_{\perp}\sin^2\theta\rangle_{\theta}/V}{\varepsilon_h - p\langle L_{\parallel}\alpha_{\parallel}\cos^2\theta + L_{\perp}\alpha_{\perp}\sin^2\theta\rangle_{\theta}/V},\\ \varepsilon_{\mathrm{eff}}^{x,y} &= \varepsilon_h + \varepsilon_h\frac{p\langle\alpha_{\parallel}\sin^2\theta + \alpha_{\perp}(2-\sin^2\theta)\rangle_{\theta}/2V}{\varepsilon_h - p\langle L_{\parallel}\alpha_{\parallel}\cos^2\theta + L_{\perp}\alpha_{\perp}(2-\sin^2\theta)\rangle_{\theta}/2V}.\end{aligned} \tag{15}$$

For ADF(θ) $= \delta(\theta)$ the result is identical to that of a nematic array [Eq. (1)], and for ADF(θ) $= 1/2$ the result is that of a random orientation (isotropic),

$$\varepsilon_{\mathrm{eff}}^{x,y} = \varepsilon_{\mathrm{eff}}^{z} = \varepsilon_h + \varepsilon_h\frac{p(2\alpha_{\perp} + \alpha_{\parallel})/3V}{\varepsilon_h - p(2L_{\perp}\alpha_{\perp} + L_{\parallel}\alpha_{\parallel})/3V}, \tag{16}$$

which coincides with the theoretical expression for random orientation [7–9].

For the third-order susceptibility, we use Eq. (5) and perform the weighted average on the hyperpolarizability, $\bar{\bar{\gamma}}$, again normalized by the volume:

$$\bar{\bar{\chi}}_{\mathrm{eff}}^{(3)} = \frac{p\langle\bar{\bar{\gamma}}/V\rangle_{\theta,\varphi}}{\varepsilon_0}. \tag{17}$$

The expression is simpler, as we assume that only the inclusions contribute to the NL response. In the general case, the fourth-rank tensor of the third-order NL susceptibility $\chi_{ijkl}^{(3)}$ can be presented as a matrix with dimensions of $[3\times 10]$ for all 32 crystallographic point groups [26]. In that case the rotation of the fields should be performed over the three interacting fields. This can be done with much more computational complication than that of the linear case. In order to maintain simplicity in the computations and the presentation of the results, we restrict ourselves to the degenerate case of a single linearly polarized input field, where the third-order NL susceptibility can be presented by an effective scalar value [26,27]. The inclusion susceptibility $\chi_i^{(3)}$ can then be extracted from the averaging in Eq. (17), and the effective susceptibility of the mixture with the averaging on the direction of the NRs will be

$$\bar{\bar{\chi}}_{\mathrm{eff}}^{(3)} = p\left\langle\left[\frac{\varepsilon_h}{\varepsilon_h\bar{\bar{\mathbf{I}}} + \bar{\bar{\mathbf{L}}}(\varepsilon_i - \varepsilon_h)}\right]^4\right\rangle_{\theta,\varphi}\chi_i^{(3)}. \tag{18}$$

The result is a second-rank tensor, because of the NRs' geometrical anisotropy, which is expressed by the directional dependency of the depolarization factor. Applying the same computation as presented for the linear permittivity, we again obtain a diagonal matrix, with two independent elements in the different directions. The results before integration over θ are

$$\begin{aligned}\chi_{\mathrm{eff}}^{(3),z} &= p\langle(f^{x,y})^4\sin^2\theta + (f^{z})^4\cos^2\theta\rangle_{\theta}\chi_i^{(3)},\\ \chi_{\mathrm{eff}}^{(3),x,y} &= p\langle 0.5(f^{z})^4\sin^2\theta + (f^{x,y})^4(1 - 0.5\times\sin^2\theta)\rangle_{\theta}\chi_i^{(3)},\end{aligned} \tag{19}$$

and we define $f^j = \varepsilon_h/[\varepsilon_h + L^j(\varepsilon_i - \varepsilon_h)]$. Again, using ADF($\theta$) $= \delta(\theta)$ will result in Eq. (5), and using ADF(θ) $= 1/2$ will result in a random orientation composite that is isotropic:

$$\chi_{\mathrm{eff}}^{(3),x,y} = \chi_{\mathrm{eff}}^{(3),z} = p[2(f^{x,y})^4 + (f^{z})^4]\chi_i^{(3)}/3. \tag{20}$$

It is important to note that we assume in all the derivations that the inclusions alone contribute to the nonlinearity (the polymer host has negligible NL susceptibility).

6. RESULTS AND DISCUSSION

In Table 3 we present an example of the composite effective permittivity and third-order NL susceptibility for the case of PFCB host and CdSe NRs with and without PDM. The results are computed from Eqs. (15) and (19) for the permittivity and NL susceptibility, respectively, after performing the integration over θ using the ADF of a 30×4.8 nm NR under different aligning field strengths. The results for the NL susceptibility are normalized by the susceptibility of the inclusions—$\chi_{\mathrm{eff}}^{(3)}/\chi_{\mathrm{CdSe}}^{(3)}$. The temperature is taken as 150°C (thermal polymerization temperature), and the volume fraction is $p = 4\%$.

Spherical inclusions with the same volume fraction of $p = 4\%$ achieve $\varepsilon_{\mathrm{eff}} = 2.2915$ and $\chi_{\mathrm{eff}}^{(3)}/\chi_{\mathrm{CdSe}}^{(3)} = 0.61\%$, orientation independent. We can see that a very strong aligning field ($>10^8$ V/m) is required for the composite to converge toward the result of the perfect nematic array, as expected. For the effective permittivity, a NR composite presents larger values than those of sphere inclusions, even for random orientation, which coincide with the theoretical prediction [see Eq. (16)]. The reason is that each component of the polarizability (each direction) contributes one third of its value to the general polarizability [7]. The permittivity in the parallel direction grows with the aligning field strength and moves away from the host permittivity value ($\varepsilon_h = 2.19$). In contrast, in the transverse direction the permittivity decreases toward the host permittivity value. At an aligning field of 10^7 V/m, for NRs with PDM, there is a small birefringence of $\Delta n = 0.0037$. For the relative third-order susceptibility we see four significant

Table 3. Comparison between the Permittivity ε_{eff} and Relative Third-Order Susceptibility $\chi^{(3)}_{\text{eff}}/\chi^{(3)}_{\text{CdSe}}$ in Parallel and Normal Directions of the Aligning Field[a]

	ε_{eff}, Effective Permittivity				$\chi^{(3)}_{\text{eff}}/\chi^{(3)}_{\text{CdSe}}$, Normalized Susceptibility			
	Without PDM		With PDM		Without PDM		With PDM	
E_{align} (V/m)	Normal	Parallel	Normal	Parallel	Normal	Parallel	Normal	Parallel
0 (random)	2.3000				1.38%			
10^6	2.3000	2.3000	2.3000	2.3001	1.38%	1.38%	1.38%	1.38%
5×10^6	2.2998	2.3005	2.2990	2.3020	1.37%	1.40%	1.33%	1.47%
10^7	2.2990	2.3020	2.2963	2.3074	1.34%	1.47%	1.21%	1.72%
5×10^7	2.2817	2.3361	2.2798	2.3398	0.54%	3.06%	0.45%	3.23%
10^8	2.2778	2.3437	2.2776	2.3442	0.36%	3.42%	0.35%	3.44%
∞ (nematic)	2.2766	2.3460	2.2766	2.3460	0.32%	3.53%	0.32%	3.53%

[a]Results for different aligning field strengths and for perfect nematic array, for NRs with and without PDM. Results for 60×3.1 nm NR, volume fraction of $p=4\%$, temperature of 150°C and PDM as calculated above.

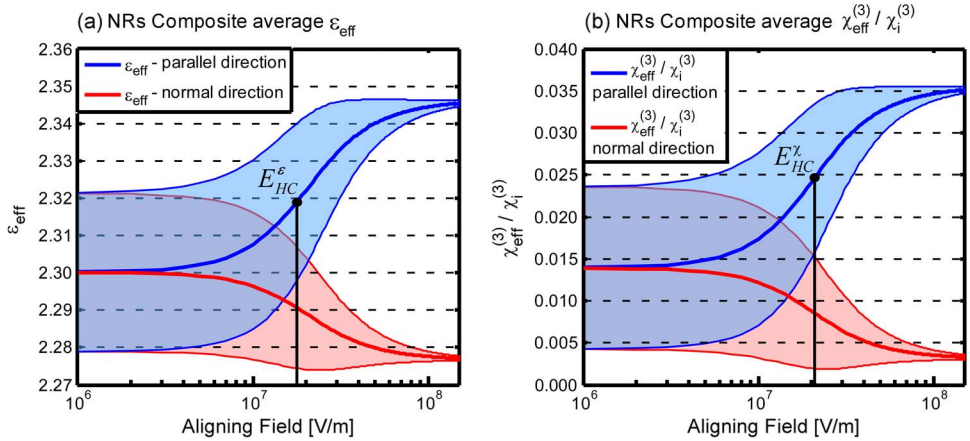

Fig. 6. Results for the average optical properties of the composite: (a) effective permittivity ε_{eff} and (b) relative third-order NL susceptibility $\chi^{(3)}_{\text{eff}}/\chi^{(3)}_{\text{CdSe}}$, as a function of the aligning field strength. Results for both the parallel (blue, upper) and transverse (red, lower) directions. Shaded areas are the average value ±1 STD.

characteristics of the composite: (1) NR composites present a much higher susceptibility than that with spherical inclusions at the same volume fraction, even without any alignment. The much higher values are because the term that consists of the depolarization factor (which is the geometrical description) is raised to the power of four [see Eq. (20)]. (2) There is a strong difference between the NL responses in each direction. (3) Even if we look at the results for a reasonable aligning field of 10^7 V/m, in the parallel direction there is an enhancement of the susceptibility, especially for the NRs with PDM. (4) In a nematic array and in strong aligning fields ($>10^8$ V/m), the relative NL susceptibility approaches the value of the volume fraction ($p=4\%$), implying a full exploitation of the inclusions' nonlinearity.

In Fig. 6 we present the average values of the effective permittivity [Fig. 6(a)] and effective third-order NL susceptibility [Fig. 6(b)], as a function of the aligning field strength, for both the parallel and the normal directions (60×3.1 nm NR with PDM). The shaded regions represent the average values ±1 standard deviation (STD), a measurement for the distribution around the average values. The STD values were calculated numerically by finding the distribution variance [28]. For both the permittivity and NL susceptibility, as the aligning field increases, the average values converge toward the nematic array values, and the STD decreases.

We define $E^{\varepsilon}_{\text{HC}}$ and E^{χ}_{HC} as the aligning field strength required in order to increase the values of the permittivity and third-order NL susceptibility, respectively, to half the change between the random orientation and the nematic array values. The values of the half-change field are presented in Figs. 6(a) and 6(b). For the NL susceptibility, as an example, without a PDM $E^{\chi}_{\text{HC}}=3.37\times10^7$ V/m (not shown), and with PDM $E^{\chi}_{\text{HC}}=2.11\times10^7$ V/m. The presence of the PDM reduced the aligning field by 37%, to reach halfway between the random and nematic composites.

7. CONCLUSION

We have presented a new geometric model for NRs, as a capsule shape, which affects the electrostatic characteristics of the NRs, mainly the polarizability and the value of the PDM that can be derived from it, and hence affects the macroscopic values of the composite permittivity and third-order NL susceptibility. We presented a method to use the polarizability of the capsule shape to find an equivalent prolate spheroid for each capsule shape, by means of the polarization density inside it. The equivalent prolate spheroid is used to find an effective value for the capsule shape depolarization factor, which enables us to use formulas for the macroscopic permittivity and third-order NL susceptibility developed analytically

for prolate spheroids. For the single particle, the capsule shape exhibits lower polarization density, compared to an equal-axes prolate spheroid, but higher polarizability due to its larger volume. The effective permittivity and the third-order NL susceptibility of the composite increase with the AR of the single NR for a fixed volume fraction, whether prolate spheroids or capsule shapes are considered, because of the decreasing depolarization factor for higher AR shapes. When comparing the composite properties for prolate spheroids or capsule-shaped inclusions at the same volume fraction and AR, the composite properties with prolate spheroid NRs are more pronounced owing to their lower depolarization factor. Finally, we showed how to calculate the ADF of the NRs and with it to calculate the macroscopic characteristics of the composite for a nematic, partially aligned, and randomly oriented array of NRs.

The NL susceptibility of such a composite depends strongly on the directionality of the NRs in the composite. The stronger the alignment is, the larger the permittivity and third-order NL susceptibility will be, in the direction parallel to the aligning field. In order to achieve a strong alignment, NRs with PDM are required, and the larger the volume and the AR of the single NR are, the larger the induced and PDM will be; hence the alignment will be stronger. The composite will be polarization dependent, which evolves from the anisotropic geometry of the NRs. The difference between the two relevant polarizations increases with the strength of the alignment, both for the permittivity (causing birefringence) and for the NL susceptibility. An isotropic composite, without any alignment applied, will still have much stronger nonlinearity compared to a composite with nanospheres.

REFERENCES AND NOTES

1. F. Trani, "Polarization anisotropy in the optical properties of silicon ellipsoids," Surf. Sci. **601**, 2702–2706 (2007).
2. J. Valenta, B. Bruhn, and J. Linnros, "Polarization of photoluminescence excitation and emission spectra of silicon nanorods within single Si/SiO_2 nanowires," Phys. Status Solidi C **8**, 1017–1020 (2011).
3. Y. K. Olsson, G. Chen, R. Rapaport, D. T. Fuchs, V. C. Sundara, J. S. Steckel, M. G. Bawendi, A. Aharoni, and U. Banin, "Fabrication and optical properties of polymeric waveguides containing nanocrystalline quantum dots," Appl. Phys. Lett. **85**, 4469–4471 (2004).
4. G. Chen, R. Rapaport, D. T. Fuchs, L. Lucas, A. J. Lovinger, S. Vilan, A. Aharoni, and U. Banin, "Optical gain from InAs nanocrystal quantum dots in a polymer matrix," Appl. Phys. Lett. **87**, 251108 (2005).
5. C. Sciancalepore, T. Cassano, M. L. Curri, D. Mecerreyes, A. Valentini, A. Agostiano, R. Tommasi, and M. Striccoli, "TiO_2 nanorods/PMMA copolymer-based nanocomposites: highly homogeneous linear and nonlinear optical material," Nanotechnology **19**, 205705 (2008).
6. J. M. Lamarre, F. Billard, and L. Martinu, "Local field calculations of the anisotropic nonlinear absorption coefficient of aligned gold nanorods embedded in silica," J. Opt. Soc. Am. B **25**, 961–971 (2008).
7. H. Sihvola, *Electromagnetic Mixing Formulas and Applications* (Institution of Engineering and Technology, 2008).
8. S. Giordano, "Effective medium theory for dispersions of dielectric ellipsoids," J. Electrost. **58**, 59–76 (2003).
9. H. Sihvola and J. A. Kong, "Effective permittivity of dielectric mixtures," IEEE Trans. Geosci. Remote Sens. **26**, 420–429 (1988).
10. B. Weintraub, Y. Deng, and Z. L. Wang, "Position-controlled seedless growth of ZnO nanorod arrays on a polymer substrate via wet chemical synthesis," J. Phys. Chem. C **111**, 10162–10165 (2007).
11. C. Lai, Y. J. Lee, P. H. Yeh, and S. W. Lee, "Formation mechanism of SiGe nanorod arrays by combining nanosphere lithography and Au-assisted chemical etching," Nanoscale Res. Lett. **7** 140 (2012).
12. J. L. Baker, A. Widmer-Cooper, M. F. Toney, P. L. Geissler, and A. P. Alivisatos, "Device-scale perpendicular alignment of colloidal nanorods," Nano Lett. **10**, 195–201 (2010).
13. L. S. Li and A. P. Alivisatos, "Semiconductor nanorod liquid crystals and their assembly on a substrate," Adv. Mater. **15**, 408–411 (2003).
14. H. E. Ruda and A. Shik, "Nanorod dynamics in ac electric fields" Nanotechnology **21**, 235502 (2010).
15. M. Shim and P. Guyot-Sionnest, "Permanent dipole moment and charges in colloidal semiconductor quantum dots," J. Chem. Phys. **111**, 6955–6964 (1999).
16. N. Venkatram, R. Sathyavathi, and D. Narayana Rao, "Size dependent multiphoton absorption and refraction of CdSe nanoparticles," Opt. Express **15**, 12258–12263 (2007).
17. J. C. Maxwell Garnett, "Colours in metal glasses and in metallic films," Philos. Trans. R. Soc. London Ser. A **203**, 385–420 (1904).
18. J. E. Sipe and R. W. Boyd, "Nonlinear susceptibility of composite optical materials in the Maxwell Garnett model," Phys. Rev. A **46**, 1614–1629 (1992).
19. L. D. Landau and E. M. Lifshitz, "A dielectric ellipsoid," in *Electrodynamics of Continuous Media*, 2nd ed. (Pergamon, 1984), pp. 39–42.
20. C. Pecharromán, J. Pérez-Juste, G. Mata-Osoro, L. M. Liz-Marzán, and P. Mulvaney, "Redshift of surface plasmon modes of small gold rods due to their atomic roughness and end-cap geometry," Phys. Rev. B **77**, 035418 (2008).
21. C. Sönnichsen and A. P. Alivisatos, "Gold nanorods as novel nonbleaching plasmon-based orientation sensors for polarized single-particle microscopy," Nano Lett. **5**, 301–304 (2005).
22. L. S. Li and A. P. Alivisatos, "Origin and scaling of the permanent dipole moment in CdSe nanorods," Phys. Rev. Lett. **90**, 097402 (2003).
23. T. Nann and J. Schneider, "Origin of permanent electric dipole moments in wurtzite nanocrystals," Chem. Phys. Lett. **384**, 150–152 (2004).
24. Ruda and Shik calculated the ADF with the integration in the denominator over the interval $[0, 2\pi]$. When examining the whole three-dimensional characteristics of the composite, θ is defined over the interval $[0, \pi]$.
25. The integration for θ is over $d(\cos\theta) = \sin\theta \cdot d\theta$. See, for example, the denominator of Eq. (7).
26. X. L. Yang and S. W. Xie, "Expression of third-order effective nonlinear susceptibility for third-harmonic generation in crystals," Appl. Opt. **34**, 6130–6135 (1995).
27. R. W. Boyd, "The intensity-dependent refractive index," in *Nonlinear Optics*, 2nd ed. (Academic, 2003), pp. 189–236.
28. The variance is the integration of the square of the relevant function (permittivity or susceptibility) minus its mean value. The STD is the square root of the variance.